ChemPubSoc Europe

DOI: 10.1002/slct.201801849

Chemistry SELECT Full Papers

Materials Science inc. Nanomaterials & Polymers

Structural Elucidation of Covalent Organic Polymers (COP) and Their Linker Effect on Gas Adsorption Performance via Density Functional Theory Approach

Santiago Aparicio,*[a] Cafer T. Yavuz,[b] and Mert Atilhan*[c, d]

Investigation of the binding affinity gases on porous adsorbents are important for establishing understanding of effective carbon dioxide adsorption and design target specific sorbents for capturing hazardous gases for environmental protection and fuel upgrading. A Density Functional Theory (DFT) study that highlights the impact of covalent organic polymer (COP) design has been conducted to explain the molecular and electronic structure, investigate the interaction sites and elucidate the experimental findings on carbon dioxide (CO_2) and nitrogen (N_2) sorption on these porous structures. DFT calculations were used to infer the details of the type and the strength of the polymer – gas interaction modes at various interaction sites as well as to quantify short-range interactions between the polymer – gas via topological characteristics analysis of intermolecular forces. Results obtained in this study were used to shed light on CO_2 and N_2 affinity of the studied polymer structures; interpretations regarding to the macroscopic behaviors were discussed and conclusions were attained on the characteristics of the adsorption type and mechanism.

1. Introduction

Unprecedented consumption amounts of the carbon based fuels have been causing the excessive release of carbon dioxide (CO_2) to atmosphere, which have caused the atmospheric CO_2 concentration levels to reach highest ever values that is known as so-called no-turning-back limits[1–2] and believed to trigger severe and extraordinary climate effects in due course unless preventive measures are taken.[3–4] Majority of the toxic emissions are caused by the industrial activities and thus in order to mitigate the release of hazardous toxic emissions to atmosphere, top priority must be given to control, reduce and eventually eliminate the gaseous emissions to atmosphere.[5] Until ultimate clean energy production processes are available, rectifications on the existing processes must be implemented in order to reduce the CO_2 emissions (and other toxic emissions) down to permissible limits by introducing new and effective CO_2 capture technologies in chemical industries as an alternative to current problematic CO_2 capture methods.[6–9] This task is known to be one of the grand challenges of the 21st century and it requires developing strategic methods (technically, economically and politically) in order to establish the tools, materials and eventually processes to tackle this major problem that affects the globe as whole.[10–12]

Both industry and academia have been investing considerably on the research efforts to elucidate of this problem, especially in the last couple of decades, and seeking for alternative materials to well-known current state-of-the-art amine based CO_2 management processes. Needless to say, besides their technical abilities to capture CO_2, researched materials must meet economic criteria in order to consider them as sustainable alternatives. Therefore, solid adsorbents have been considered for this purpose, despite most of the current capture infrastructure is based on liquid state amine based absorbents. Regardless of either adsorbents or absorbents, capture materials must include the characteristics of null (or minimum) toxicity,[13] low corrosivity,[14–16] low regeneration cost[17–21] and low degradation properties.[22–24] There is an increasing interest on some new alternative materials that are considered as alternative CO_2 capture solvents such as ionic liquids[25] and deep eutectic solvents.[26–27]

The properties of these materials might meet the qualifications for high-performance absorbents that can work based on either chemical or physical sorption mechanism depending on the selection of constituents of the solvents. Furthermore, other alternative adsorbents such as membranes,[28] metal organic frameworks,[29–30] covalent organic frameworks,[31–32] porous polymers or other porous materials[33–34] have been considered for the same intended purpose. For either absorbents and adsorbents, the most challenging issue in industrial scale for a sorbent that can be considered as an alternative in a fossil-fueled power plant (or other chemical industry that has high CO_2 emissions) is the low CO_2 partial pressures that requires

[a] Prof. S. Aparicio
Department of Chemistry, University of Burgos, 09001 Burgos, Spain
E-mail: mert.atilhan@tamu.edu
[b] Prof. C. T. Yavuz
Korean Advanced Institute of Science and Technology (KAIST), Daejeon, S. Korea
[c] Prof. M. Atilhan
Department of Chemical Engineering, Texas A&M University at Qatar, Doha, Qatar
E-mail: sapar@ubu.es
[d] Prof. M. Atilhan
Gas and Fuels Research Center, Texas A&M University, College Station, TX, USA

Supporting information for this article is available on the WWW under https://doi.org/10.1002/slct.201801849

high efficiency capture performance for less sorption energy penalty.[35] Therefore, gas sorption and effective separation process should be based mainly on physisorption with pressure swing regeneration.

According to above-mentioned constraints, covalent porous adsorbents[36–38] have received remarkable attention in recent years due to their structures that allows multiple alternatives for custom design and engineering in order to achieve high CO_2 adsorption performance that can support high gas selectivity with low energy cost regeneration properties in comparison to toxic and corrosive amine solutions[24,39] Powerful and ever-expanding methods could be provided by molecular and polymer synthesis methods that can result in outstanding chemical selectivity, stereospecifity, control of polymer composition, size and architecture for the targeted intended utilization of these materials.[40] Having said that, covalent porous organic polymers (CPOP) have structures that include attractive high-affinity CO_2 (and other gases depending on the structure) interaction sites with low-to-moderate binding energies. COPs, mostly amorphous insoluble powder materials with few exceptions, are synthesized to have relatively high surface area, adjustable pore dimensions and low densities that are essential for utilization as gas storage medium, catalysis and other relevant applications.[41–42] Physisorption based adsorption mechanism of amorphous COPs might lead to considerably lower regeneration energies in contrast with metal organic frameworks.[43]

COP synthesis involves connecting molecular building blocks, cores and linkers, during polymerization processes, and with its covalently bonded structure they confer very good chemical integrity, stability and high thermal stability that are achieved via synthesis process via powerful approach to access 2D and 3D polymer networks with the method that include directional bonding of COP monomers leads to supramolecular assemblies and coordination polymers.[44–52] The shape of the monomer (cores and linkers) determines the topology and gas attraction site of the final structure in the case of it is utilized for gas adsorption.

Patel et al. has shown that COPs that are built with azo group (–N=N–) have very high thermal stability, large surface area, can store vast amount of CO_2 with high counter N_2 selectivity.[53] Comparing the production cost and CO_2 capturing capacity at high pressure up to 200 bars of COP-1 to that of MEA solution, Patel et al.[31] has also suggested that COPs could store significantly high amount of CO_2 at low economic cost. (CO_2 uptake amount with 5616 mg/g for COP-1[31] and with 3294 mg/g for COP-3[54] at 318 K and 200 bar.[54] Z. Xiang et al.[55] has tested several COPs for adsorption of O_2, N_2, H_2 and CH_4 and showed that COP-4 can adsorbed 594 mg/g of CO_2 at 298 K and 18 bars. Gomes et al.[56] and Modak et al.[57] have worked on triazine functionality based COPs that are hexagonally ordered. Gomes et al. produced COP named TRITER-1 that was synthesized via the Schiff-base condensation reaction between a tailor made triamine 1,3,5-tris-(4-aminophenyl) triazine (TAPT) and terephthaldehyde and this work yielded COP with high BET surface area (716 m^2/g) and an excellent CO_2 uptake capacity of 58.9 wt% at 273 K at 5 bar.[56] Furthermore, Modak et al. have synthesized on a similar work a COP named TPOP-1, which showed excellent CO_2 storage capacity (6.2 mmol/g or 27.3 wt% at 3 bar/273 K), suggesting its potential application in environmental clean-up.[57]

Although there have been many studies that investigates the CO_2 (and other gases) capture and separation performance of COPs in recent years, efforts seems to be concentrated mostly on the design, synthesis and experimental aspects.[31,58–61] There are very rare studies that include theoretical approach on COPs for explaining how CO_2 (or other gases) binding occur with proper quantification in molecular level and making links to experimental findings to explain how COPs function in both macroscopic and bulk phases and seeks the impact of designed COP at the molecular and electronic levels on the gas attraction and binding affinity at the molecular interaction sites in the case of different core and linker elements employed.

According to open literature, there is no available work fully on theoretical aspects, which is dedicated to investigate the COP structure gas interaction properties via nanoscopic approach. Therefore, in this work, we investigated on the gas sorption performances at various sorption sites via density functional theory (DFT) approach of two previously[62] synthesized COPs that includes 1,3,5-benzene tricarbonyltrichloride as core. Amide based 4-aminobenzylamine linker was used to produce COP-32 and ester based hydroquinone linker was used to produce COP-35. The aim of this paper is to investigate the effect of linker type and the binding cites on the performance of COP – gas interaction by using computational quantum mechanical modeling methods. Details of the study are given below.

2. Methods

Structures

Two COP structures, namely COP32 (representing amide based COPs) and COP35 (representing ester based COPs) were considered based on our groups previous work[62] (Figure 1). Molecular clusters containing COP32 + CO_2, COP32 + N_2, COP32 + CO_2 + N_2, COP35 + CO_2, COP35 + N_2, COP35 + CO_2 + N_2 were studied by considering four different CO_2 and N_2 spatial positions to infer interaction properties at all logical active sites of the studied COP molecules (e.g. p1, p2, p3, p4 positions selected as potential gas interaction) as can be seen in Figure 1. For COP32, p1 site is located between =O and -NH at the center of the core structure (benzene tricarbonyl trichloride), p2 site is right below the -NH group located at the core, p3 site is located at the top of the benzene ring of the linker (4-aminobenzylamine) and p4 site is located at the top of the benzene ring of the core. Whereas for COP35, p1 site is next to –O and p2 site is next to =O groups for the core structure (benzene tricarbonyl trichloride), p3 site is located at the top of the benzene ring of the linker (hydroquinone) and p4 site is located at the top of the benzene ring of the core. Figure 1 in shows these selected interaction sites.

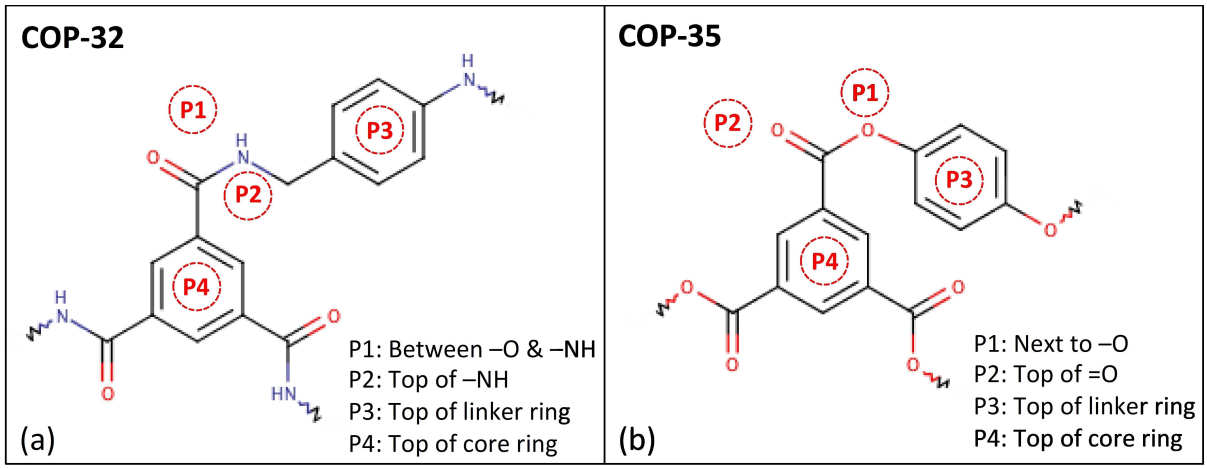

Figure 1. Studied COP structures marked with gas molecule positions that are used during DFT simulations: (a) COP-32 and (b) COP-35.

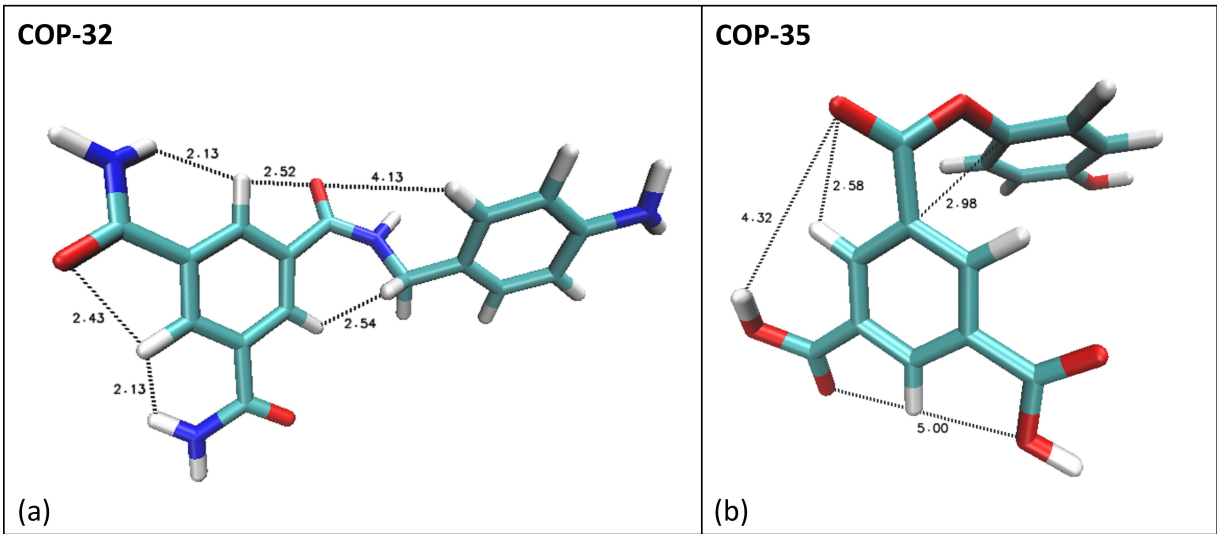

Figure 2. Final geometry of structures optimized with B3LYP 6–311++G** theory level: (a) COP-32 and (b) COP-35. (Numbers are in Å and indicate the distance between selected atoms)

DFT Methods

Initial molecular structures were built by using Avogadro program[63] and DFT simulations were performed by using ORCA software.[64] All the calculations were done with the B3LYP functional[65–66] together with the DFT–D3 method by Grimme,[67] for considering dispersion interactions, and the 6–311++G** basis set (i.e. B3LYP/6- 311++G** theoretical level). The details of the used DFT methods and analysis techniques are provided in ESI.

3. Results

Final optimized geometries of COP32 and COP35 compounds were achieved with B3LYP 6–311++G** theory level and the final optimized structures for these compounds are provided in Figure 2a (COP32) and in Figure 2b (COP35). Critical bond lengths were measured and shown in Figure 2 for structural analysis of the final optimized geometries of both COPs. According to Figure 2, both COPs have been bent from the location at which linkers were added to the core molecule. The bending point for COP32 is p2 and for COP35 is p1.

Experimental FTIR values compared with calculated spectroscopic values with DFT simulations are provided in Figure S1, in Electronic Supporting Information (ESI). It would be beneficial to show the IR spectra that are obtained both via theoretically and experimentally, is shown in Figure S1. The theoretical and experimental IR spectra were recorded on a Shimadzu IR-Tracer-100 equipped with a Gladi ATR module previously [ref]. Theoretical IR spectra of the most stable COP geometries were obtained by using molden files processed in Multiwfn program code.[68] Examination of Figures S1 shows that the experimental IR spectra of the studied compound are mostly similar to those obtained via DFT calculations for

isolated COPs. However, it would not be realistic to expect comprehensive similarities between experimental and theoretical IR frequencies for the isolated molecule and this could be explained due to the effect of the hydrogen bonding interaction in the solid-state spectra. The highest frequency experimental bands observed in the IR spectrum are assigned to the aromatic C–H stretches, while the lower frequency bands are attributed to the methyl group motions. The (C–H) bands are of low intensity in both the experimental and theoretical spectra.

Density-of-states (DOS) is an important concept, which represents the number of states in unit energy interval, since energy levels are contiguous. Therefore DOS can be plotted as curve map. If the discrete energy levels are broadened to curve artificially, DOS graph can be used as a valuable tool for analyzing the nature of electron structure. DOS as a function of orbital energy, E, for both optimized structures of COP32 and COP35 were calculated at B3LYP/6-311++g(d,p) level and they are reported in Figure S2. From the height of black curve for COP32 and red curve for COP35 (DOS traces were shifted for the sake of visibility), we can clearly know how dense the energy levels are distributed everywhere. The blue dashed lines highlights on DOS plot shows position of HOMO and LUMO. The curve is the DOS simulated based on the distribution of molecular orbital (MO) energy levels. The negative part has obviously larger state density than positive region. Furthermore, DOS results as a function of E for both COP32 and COP35 interaction with each gas and each position are also reported in Figure S3. Broadening of the DOS plot peaks can be attributed to hybridization when the orbitals of the adsorbate and the layer hybridized. Broadening can also be attributed to van der Waals (vDW) interactions of the COPs with gas molecules in the studied cases. Shifting of the peak corresponds to changing behavior of substance.

Frontier molecular highest occupied molecular orbital (HOMO), lowest unoccupied molecular orbital (LUMO) orbitals for COP32 and COP35 monomers were calculated at B3LYP/6-311++ g(d,p) level and presented in Figure S4 (positive (blue) and negative (red) isosurfaces). The HOMO/LUMO gap of a polymer is calculated as the minimum difference between the HOMO and the LUMO energy levels at a given k-point.

The energy levels of the HOMO and LUMO are calculated as the maximum of the HOMO and the minimum of the LUMO respectively and these results are also presented in Table 1.

The appropriate HOMO/LUMO energy level of the donors and acceptors, and low band-gap are known to be important for high strong absorption ability, and high charge mobility. HOMO–LUMO gaps that are presented in Table 1 shows that most of the values for all studied cases including COPs by itself and COPs interacting with other gas molecules are approximately in the range of 2.5 to 4.1 eV. These values can be considered as close to the visible region, which refers to the light absorption the UV region. And such energy gap values also represents that the studied structures are highly stable. For COP32, HOMO is located at the linker and LUMO is located at the core side, as per Figure S4a and Figure S4b. Similar trend is also observed for COP35, Figure S4c and Figure S4d. Furthermore, HOMO/LUMO orbitals for best adsorption performing cases of COP32 and COP35 are also presented in Figure S5 and Figure S6 respectively. For COP32_CO_2_p1 case HOMO is at the linker (Figure S5a) and LUMO is at the core (Figure S5d) side. Same trend is observed for COP32_N_2_p2 (Figure S5b and Figure S5e), and also for COP32_CO_2_ N_2_p2 (Figure S5c and Figure S5f) cases. When COP35 is analyzed for gas adsorption cases, same trends that was observed for COP32 is recorded in Figure S6a-f.

Table 1. Properties of COP32 and COP35 systems that are calculated at B3LYP/6-311++g(d,p)theory level. Counterpoise corrected interaction energy (ΔE); gas binding energies (E_{bind}); HOMO (E_{HOMO}) and LUMO (E_{LUMO}) energies; HOMO-LUMO energy gap (ΔE_G).

Structure	E_{int} / eV	$E_{bind.}$ / eV	E_{HOMO} / eV	E_{LUMO} / eV	ΔE_G / eV
COP32	-	-	-5.1977	-1.8378	3.3599
COP32-CO_2-p1	-0.1285	-0.1285	-5.9359	-1.8783	4.0576
COP32-CO_2-p2	-0.0161	-0.0161	-5.8934	-1.8245	4.0689
COP32-CO_2-p3	-0.0472	-0.0472	-5.8183	-1.8168	4.0015
COP32-CO_2-p4	-0.0399	-0.0399	-5.1083	-2.5161	2.5922
COP32-N_2-p1	-0.0187	-0.0187	-5.8990	-1.8229	4.0761
COP32-N_2-p2	-0.0199	-0.0199	-6.0775	-4.1321	1.9454
COP32-N_2-p3	-0.0007	-0.0007	-5.9401	-1.8378	4.1023
COP32-N_2-p4	0.0000	0.0000	-5.9163	-1.8372	4.0791
COP32-CO_2-N_2-p1	-0.1582	-0.1582	-5.9163	-1.8286	4.0877
COP32-CO_2-N_2-p2	-0.1756	-0.1756	-5.9334	-1.7867	4.1467
COP32-CO_2-N_2-p3	-0.0560	-0.0560	-6.0952	-1.8642	4.2310
COP32-CO_2-N_2-p4	-0.1431	-0.1431	-5.8883	-1.8676	4.0207
COP35	-	-	-5.7002	-3.2708	2.4294
COP35-CO_2-p1	-0.1152	-0.1152	-6.6270	-2.6559	3.9711
COP35-CO_2-p1	-0.0167	-0.0167	-6.6098	-2.5424	4.0674
COP35-CO_2-p3	-0.0214	-0.0214	-6.6179	-2.6208	3.9971
COP35-CO_2-p4	-0.0166	-0.0166	-6.6096	-2.5913	4.0183
COP35-N_2-p1	-0.0223	-0.0223	-6.5880	-2.6185	3.9695
COP35-N_2-p2	-0.0097	-0.0097	-6.5597	-2.5464	4.0133
COP35-N_2-p3	-0.0049	-0.0049	-6.5871	-2.6117	3.9754
COP35-N_2-p4	-0.0096	-0.0096	-6.5582	-2.5478	4.0104
COP35-CO_2-N_2-p1	-0.0774	-0.0774	-6.6352	-2.6014	4.0338
COP35-CO_2-N_2-p2	-0.0800	-0.0800	-6.6222	-2.5572	4.0650
COP35-CO_2-N_2-p3	-0.0513	-0.0513	-6.6227	-2.5464	4.0763
COP35-CO_2-N_2-p4	-0.0245	-0.0245	-6.6052	-2.5667	4.0385

COP – CO_2/N_2 Interaction Analysis

Main results for counterpoise corrected interaction energy, ΔE; gas binding energies, E_{bind}; HOMO and LUMO energies, E_{HOMO} and E_{LUMO}; HOMO-LUMO energy gap, ΔE_G are reported in Table 1. Furthermore, considering the subject focus of this study is to investigate the effect of linker type on the interactions of COP compounds with both CO_2 and N_2 gas molecules, we also analyzed the characteristics of bonding type and strength in either single gas or both the gases coexist at the identified potential active sites (i.e. p1, p2, p3, p4) of COP adsorption sites. Numerical results for the calculated ρ and laplacian of $\nabla^2\rho$ for all studied COP – CO_2/N_2 interaction analysis cases are reported in Table 2 for COP32 and Table 3 for COP35.

AIM and RDG analysis of COP32 interaction strength and binding types are given in Figure 3 for COP32+CO_2, Figure 4 for COP32+N_2 case and Figure 5 for COP32+CO_2+N_2 cases.

Table 2. Atoms-in-a-molecule analysis of the reported COP32-CO_2-N_2 systems calculated at B3LYP/6-311++g(d,p) level. Bond critical point (BCP, (3,−1)) and ring critical point (RCP, (3,+1)) are provided in the table. Electron density (ρ) and laplacian of electron density ($\nabla^2\rho$) at the corresponding BCP and RCP are provided as a guide for AIM and RDG Figures 4, 5, 6.

Structure	Critical Point	ρ / a.u.	$\nabla^2\rho$ / a.u.
COP32-CO_2-p1	BCP1	0.1640×10^{-2}	0.3798×10^{-1}
	BCP2	0.1292×10^{-2}	0.3696×10^{-1}
	RCP1	0.8354×10^{-3}	0.2355×10^{-1}
COP32-CO_2-p2	BCP1	0.6613×10^{-3}	0.1714×10^{-1}
COP32-CO_2-p3	BCP1	0.1456×10^{-2}	0.3089×10^{-1}
COP32-CO_2-p4	BCP1	0.1648×10^{-2}	0.3814×10^{-1}
	BCP2	0.1290×10^{-2}	0.3683×10^{-1}
	RCP1	0.8349×10^{-3}	0.2354×10^{-1}
COP32-N_2-p1	BCP1	0.1203×10^{-2}	0.2227×10^{-1}
COP32-N_2-p1	BCP1	0.1264×10^{-2}	0.2306×10^{-1}
COP32-N_2-p3	RCP1	-0.2787×10^{0}	-0.9615×10^{0}
	RCP2	0.7385×10^{-2}	0.1592×10^{0}
COP32-N_2-p4	BCP1	0.3557×10^{-4}	0.3510×10^{-3}
	BCP2	0.4361×10^{-4}	0.4141×10^{-3}
	RCP1	0.3248×10^{-4}	0.3152×10^{-3}
	RCP2	0.4334×10^{-4}	0.4118×10^{-3}
COP32-CO_2-N_2-p1	BCP1	0.1394×10^{-2}	0.3312×10^{-1}
	BCP2	0.130910^{-2}	0.3797×10^{-1}
	BCP3	0.5810×10^{-3}	0.1136×10^{-1}
	BCP4	0.4616×10^{-3}	0.7419×10^{-2}
	BCP5	0.1355×10^{-2}	0.2523×10^{-1}
	RCP1	0.7901×10^{-3}	0.2283×10^{-1}
COP32-CO_2-N_2-p2	BCP1	0.1200×10^{-2}	0.2230×10^{-1}
	BCP2	0.1475×10^{-2}	0.3421×10^{-1}
	BCP3	0.8465×10^{-3}	0.2355×10^{-1}
	BCP4	0.1571×10^{-2}	0.3141×10^{-1}
	RCP1	0.7693×10^{-3}	0.1695×10^{-1}
	RCP2	0.8939×10^{-3}	0.1951×10^{-1}
COP32-CO_2-N_2-p3	BCP1	0.1113×10^{-2}	0.2709×10^{-1}
COP32-CO_2-N_2-p4	BCP1	-0.1860×10^{-2}	0.5105×10^{-3}
	BCP2	-0.5412×10^{-2}	0.1622×10^{-2}
	BCP3	-0.3184×10^{0}	-0.2830×10^{0}
	BCP4	-0.1940×10^{-2}	0.6174×10^{-3}
	BCP5	-0.3331×10^{-3}	0.1237×10^{-2}
	RCP1	-0.6104×10^{-3}	0.4326×10^{-3}
	RCP2	-0.1136×10^{-2}	0.5736×10^{-3}
	RCP3	-0.1880×10^{-2}	0.6710×10^{-2}

Table 3. Atoms-in-a-molecule analysis of the reported COP35-CO_2-N_2 systems calculated at B3LYP/6-311++g(d,p) level. Bond critical point (BCP, (3,−1)) and ring critical point (RCP, (3,+1)) are provided in the table. Electron density (ρ) and laplacian of electron density ($\nabla^2\rho$) at the corresponding BCP and RCP are provided as a guide for AIM and RDG Figures 7, 8, 9.

Structure	Critical Point	ρ / a.u.	$\nabla^2\rho$ / a.u.
COP35-CO_2-p1	BCP1	0.1275×10^{-2}	0.3012×10^{-1}
COP35-CO_2-p2	BCP1	0.2426×10^{-2}	0.4595×10^{-1}
	BCP2	0.1033×10^{-2}	0.2836×10^{-1}
	BCP3	0.1174×10^{-2}	0.2296×10^{-1}
	RCP1	0.1034×10^{-2}	0.2387×10^{-1}
COP35-CO_2-p3	-	-	-
COP35-CO_2-p4	BCP1	0.2447×10^{-2}	0.4648×10^{-1}
	BCP2	0.1022×10^{-2}	0.2808×10^{-1}
	BCP3	0.1171×10^{-2}	0.2279×10^{-1}
	RCP1	0.1035×10^{-1}	0.2381×10^{-1}
COP35-N_2-p1	RCP1	0.3704×10^{-3}	0.4765×10^{-2}
COP35-N_2-p2	BCP1	0.2191×10^{-2}	0.3914×10^{-1}
COP35-N_2-p3	BCP1	0.2126×10^{-3}	0.3353×10^{-2}
COP35-N_2-p4	BCP1	0.2194×10^{-2}	0.3912×10^{-1}
COP35-CO_2-N_2-p1	BCP1	-0.2763×10^{0}	-0.9469×10^{0}
	BCP2	0.2239×10^{-2}	0.3998×10^{-1}
COP35-CO_2-N_2-p2	BCP1	0.2394×10^{-2}	0.4523×10^{-1}
	BCP2	0.1026×10^{-2}	0.2820×10^{-1}
	BCP3	0.1195×10^{-2}	0.2355×10^{-1}
	RCP1	0.1028×10^{-2}	0.2372×10^{-1}
	RCP2	0.7465×10^{-3}	0.1621×10^{-1}
COP35-CO_2-N_2-p3	BCP1	0.2471×10^{-1}	0.4693×10^{-1}
	BCP2	0.1022×10^{-2}	0.2807×10^{-1}
	BCP3	0.1065×10^{-1}	0.2255×10^{-1}
	RCP1	0.7405×10^{-3}	0.1583×10^{-1}
COP35-CO_2-N_2-p4	BCP1	0.2189×10^{-2}	0.3911×10^{-1}
	BCP2	0.4296×10^{-3}	0.8013×10^{-2}

All these figures, and other figures that contain AIM and RDG data, include the visual representations for BCPs (type (3,−1)) and RCPs (type (3,+1)) that are calculated according to Bader's theory.[69]

Please note that as per AIM theory, for hydrogen bonding ρ and $\nabla^2\rho$ must be in the range 0.002 to 0.04 a.u. and 0.020 to 0.139 a.u, respectively.[70] In RDG iso-surface information containing figures, green or green-brown color indicates van der Waals type interactions between the gas molecule and the sorption site.

For COP32+CO_2 case, highest interaction yielding case is observed to be occurring at p1 (located between =O and -NH) and p4 (located at the top of the benzene ring) sites with same ρ and $\nabla^2\rho$ results ($\rho=0.164\times10^{-2}$ and $\nabla^2\rho=0.379\times10^{-1}$ a.u. for COP32-CO2-p1 at BCP1; $\rho=0.164\times10^{-2}$ a.u. and $\nabla^2\rho=0.381\times10^{-1}$ a.u. for COP32-CO_2-p4 at BCP1), as shown in Table 2. According to ρ and $\nabla^2\rho$ values, interactions can be characterized as vDW type and they are very close to lower boundary of H-bonding, which are also evidenced by the RDG images in Figure 3e and Figure 3h with green-brownish isosurfaces. In these figures, the distance between CO_2 and the interacting site is measured as 2.31 Å and the C–CO angle for CO_2 is measured with minor deformation and bending as 177.26° indicating physisorption behavior.

Upon close inspection at Figure 3a and Figure 3d, one can see that the final optimized positions of CO_2 is very similar to each other and thus explaining the similar ρ and $\nabla^2\rho$ results given above. It seems like the when CO_2 is placed at the top of the benzene ring, p4, intermolecular forces pushed CO_2 to exact same position at which CO_2 is located at optimized p1 case. As can be seen in Figure 3a and Figure 3d, BCP1 corresponds to N–H binding site located at the core-linker connection point. Thus, one can conclude that the COP32+CO_2 interaction is being dominated with this functional group, which came from 4-aminobenzylamine linker. On the other hand, both COP32-CO_2-p2 and COP32-CO_2-p3 represented CO_2 interaction at linker molecule with only 1 obtained BCP. There is remarkable difference with ρ values for these two cases with 0.661×10^{-3} a.u. and 0.145×10^{-2} a.u. for COP32-CO_2-p2 and COP32-CO_2-p3 respectively, placing the bonding type outside H-bonding region and observed to be vDW type interactions. For the bond strength for these two cases, $\nabla^2\rho$ are recorded as 0.171×10^{-1} a.u. and 0.308×10^{-1} a.u. for COP32-CO_2-p2 and COP32-CO_2-p3 respectively.

For COP32+N_2 case, highest interaction yielding case is observed to be occurring at both p1 and p2 positions (Table 2). Similar to COP32+CO_2 case, upon close inspection at Figure 4a and Figure 4b, final optimized positions of N_2 is very similar to each other and thus explaining the similar ρ and $\nabla^2\rho$ results as

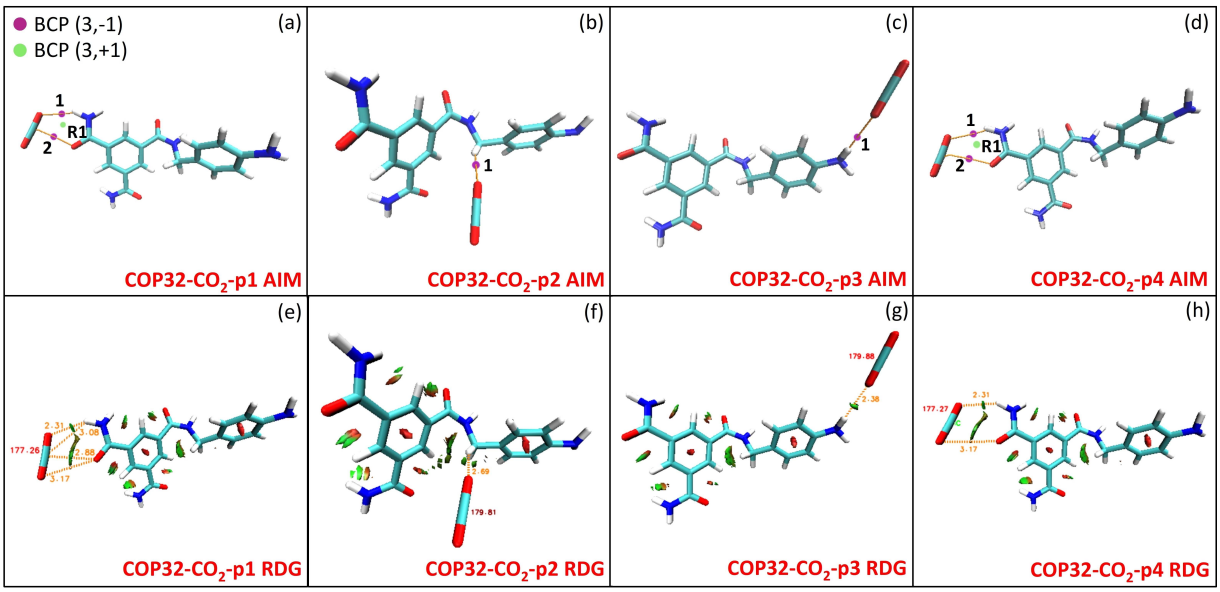

Figure 3. Atom in Molecule (AIM) analysis of COP32 interaction with CO_2 at P1-P2-P3-P4 positions at figure panels a, b, c, d. Bond critical points (BCP) and ring critical points (RCP) involving COP32–CO_2 interactions according to AIM are shown. Reduced Density Gradient (RDG) iso-surfaces (green or green-brown color indicates van der Waals interactions) at figure panels e, f, g, h.

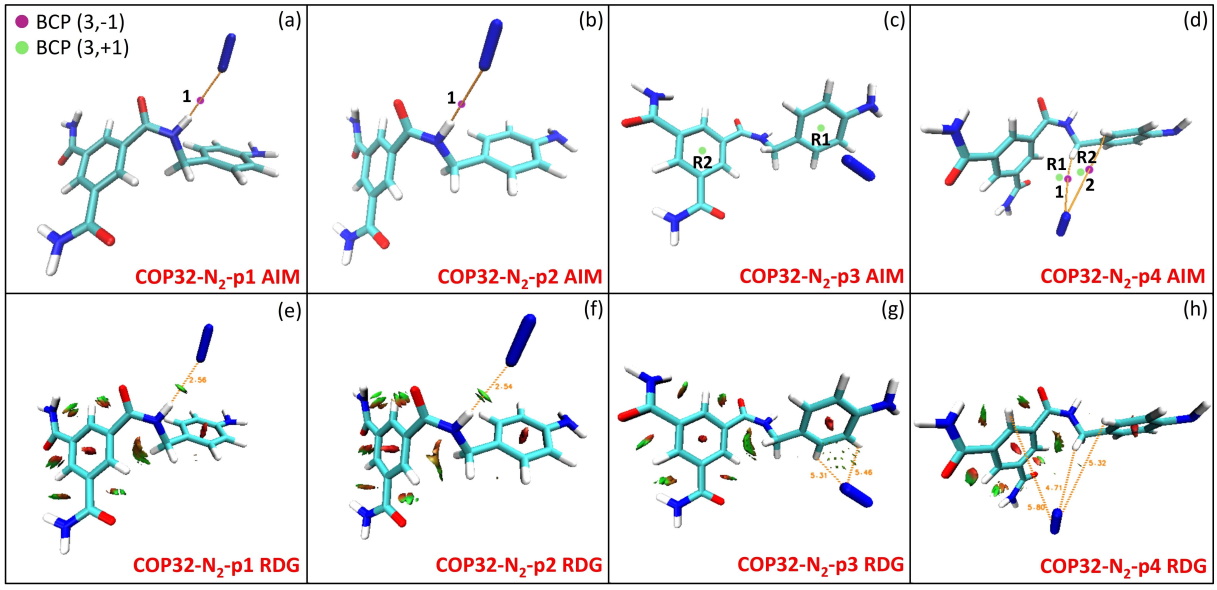

Figure 4. Atom in Molecule (AIM) analysis of COP32 interaction with N_2 at P1-P2-P3-P4 positions at figure panels a, b, c, d. Bond critical points (BCP) and ring critical points (RCP) involving COP32–N_2 interactions according to AIM are shown. Reduced Density Gradient (RDG) iso-surfaces (green or green-brown color indicates van der Waals interactions) at figure panels e, f, g, h.

$\rho = 0.120 \times 10^{-2}$ a.u. and $\nabla^2\rho = 0.222 \times 10^{-1}$ a.u. for COP32_N_2_p1 and $\rho = 0.126 \times 10^{-2}$ a.u. and $\nabla^2\rho = 0.230 \times 10^{-1}$ a.u. for COP32_N_2_p2. It seems like the when N_2 is placed at the p1 position, intermolecular forces pushed N_2 to exact same position at which N_2 is located at optimized p2 case. For both COP32_N_2_p1 and COP32_N_2_p2 cases, dominating interaction is located at –NH group that is located in the 4-aminobenzyl-amine linker as well. According to ρ and $\nabla^2\rho$ values, interactions can be characterized as vDW type and they are at the lower boundary of H-bonding, which are also evidenced by the RDG images in Figure 4e and Figure 4f with green-brownish isosurfaces. N_2 distance to the –NH interaction site is measured as 2.54 Å. Interestingly there was no BCP recorded for the case of COP32_N_2_p3 case, for which final position of N_2 is located on the top the benzene ring of the linker molecule, Figure 4c.

More complicated interactions were observed for the case of when both CO_2 and N_2 were simulated together with COP32 (COP32 + CO_2 + N_2 case). Results for this study is provided in

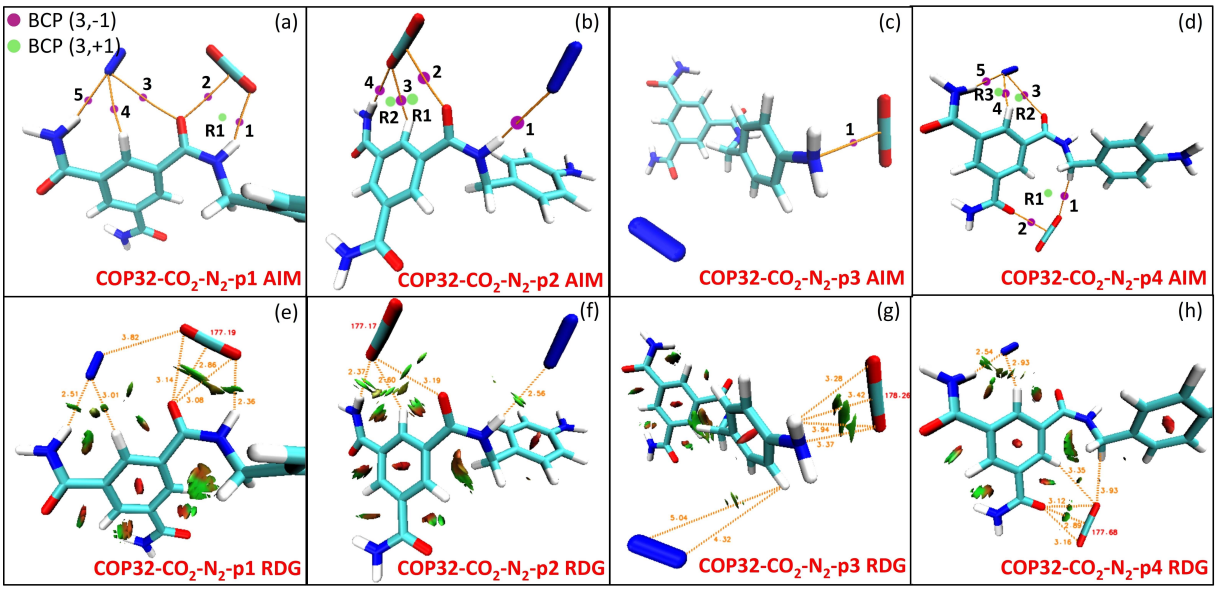

Figure 5. Atom in Molecule (AIM) analysis of COP32 interaction with CO_2 and N_2 at P1-P2-P3-P4 positions at figure panels a, b, c, d. Bond critical points (BCP) and ring critical points (RCP) involving COP32–CO_2–N_2 interactions according to AIM are shown. Reduced Density Gradient (RDG) iso-surfaces (green or green-brown color indicates van der Waals interactions) at figure panels e, f, g, h.

Figures 5a to 5 h. For p1, p2 and p4 interaction cases, both CO_2 and N_2 showed interactions with COP32 molecule, whereas for P3 case only CO_2 interaction was recorded. BCPs values can be ranked for each positions as: *i)* for p1 BCP1 > BCP5 > BCP3 ≫ BCPs3-4; *ii)* for p2 BCP4 > BCP2 > BCP1 ≫ BCP3; *iii)* for p4 BCP2 ≫ BCP1 > BCP3 > BCP4 > BCP5. According to numerical ρ and $\nabla^2\rho$ values, it was observed that CO_2 interaction with COP seems to be stronger than that of N_2 interactions for all studied positions, which is an important indication for CO_2/N_2 separation applications. Among the four cases, p2 case has the highest ρ and $\nabla^2\rho$ values for CO_2 interaction case with 0.157×10^{-2} a.u. and 0.314×10^{-1} a.u. respectively observed at BCP4.

Table 2 values indicate some negative values for ρ and $\nabla^2\rho$, which needs further explanation. The regions where $\nabla^2\rho$ is observed to be negative, ρ is locally greater than the average value in the near neighborhood of BCP in these regions is thought to be locally concentrated. On contrary, for the regions where $\nabla^2\rho$ is positive, ρ is locally less than the average value near BCP can be claimed as locally depleted in these regions. The region where $\nabla^2\rho$ is negative includes the inter-nuclear region as well as the valence shell regions of both atoms forming an adjoining domain of local charge concentration that covers the interatomic surface. Besides, $\nabla^2\rho$ can be considered as positive over the inter-nuclear region that contains BCP, and it can be considered negative in the region of the valence shell of the more electronegative atom where ρ is locally concentrated. Finally, the sign of $\nabla^2\rho$ should change from positive to negative as $\nabla^2\rho$ decreases.

Having discussed COP32 interactions with CO_2 and N_2, we move on to COP35 interactions and to start with when COP35 + CO_2 interactions are analyzed for ρ and $\nabla^2\rho$ at studied positions, it was observed at two cases namely COP35_CO_2_p2 at BCP1 and COP35_CO_2_p4 at BCP1 yields the strongest binding interaction cases with very close ρ values of 0.242×10^{-2} a.u. and 0.244×10^{-2} a.u. and $\nabla^2\rho$ values as 0.459×10^{-2} a.u. and 0.464×10^{-2} a.u. respectively; placing the both interactions at the lower boundary of hydrogen bonding region. Essentially, when both p2 and p4 cases are analyzed in Figures 6b and 6d, both optimized geometries resulted in same molecular orientation with CO_2 located at similar distance and location relative to COP35 structure with highest CO_2 interaction occur between C(CO_2) and –OH site. For both p2 and p4 cases, RDG isosurfaces at BCP1 vicinity shows greenish-brownish colors that confirms the ρ and $\nabla^2\rho$ values being close to the lower boundary of H-bonding zones as per AIM theory; Figures 6f and 6 h. –OH site in the final COP35 structure is due to the ester based Hydroquinone linker molecule and the presence of it seems to dominate the CO_2 interaction for COP35. When CO_2 is placed on the top of benzene ring that is located in the linker, there is no notable BCP and thus interaction is recorded for COP35_CO_2_p3 case. Distance between C (at CO_2) and H (at –OH) is recorded to be 2.20 Å and C–CO angle is 178.39°.

AIM and RDG results for the case of COP35 + N_2 are provided in Figures 7a to 7 h. COP35_N_2_p1 did not result a BCP due to low interactions between COP35 and N_2 molecules. COP35_N_2_p3 case yielded lowest ρ values with 0.212×10^{-3} a.u. meaning weak vDW interactions between N_2 and benzene ring located at the linker side. For both COP35_N_2_p2 and COP35_N_2_p4 cases a very similar ρ and $\nabla^2\rho$ values obtained at only BCPs (BCP1), $\rho = 0.219\times10^{-2}$ a.u. and $\nabla^2\rho = 0.391\times10^{-2}$ a.u. exactly same for both p2 and p4 cases. These interactions are observed to occur between –N and –OH sites.

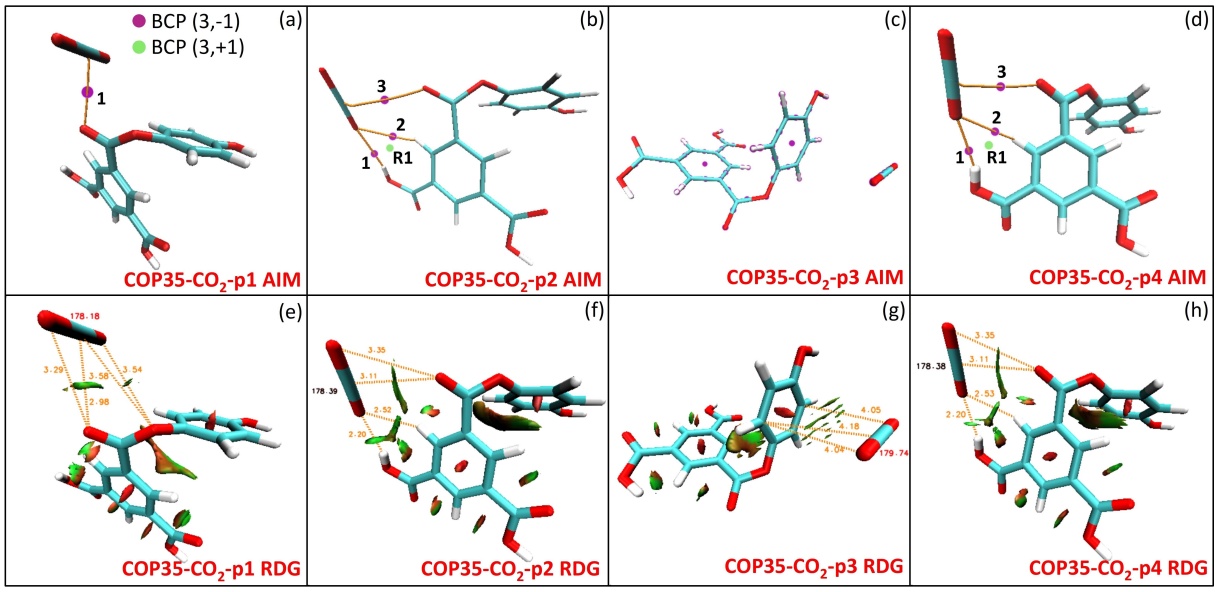

Figure 6. Atom in Molecule (AIM) analysis of COP35 interaction with CO_2 at P1-P2-P3-P4 positions at figure panels a, b, c, d. Bond critical points (BCP) and ring critical points (RCP) involving COP35–CO_2 interactions according to AIM are shown. Reduced Density Gradient (RDG) iso-surfaces (green or green-brown color indicates van der Waals interactions) at figure panels e, f, g, h.

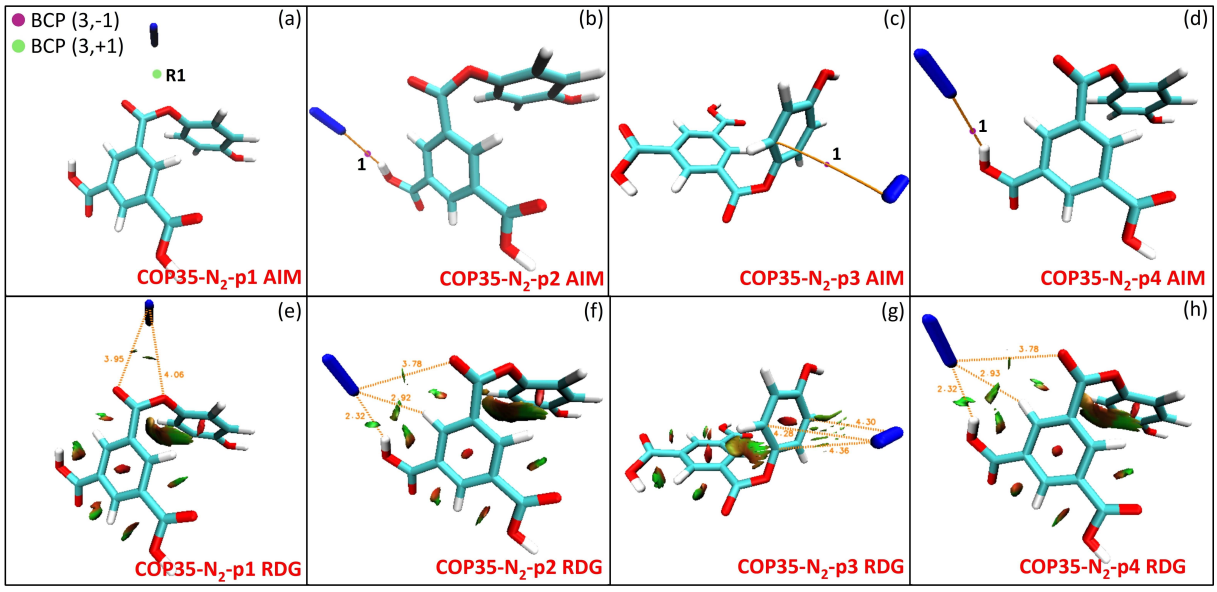

Figure 7. Atom in Molecule (AIM) analysis of COP35 interaction with N_2 at P1-P2-P3-P4 positions at figure panels a, b, c, d. Bond critical points (BCP) and ring critical points (RCP) involving COP35–N_2 interactions according to AIM are shown. Reduced Density Gradient (RDG) iso-surfaces (green or green-brown color indicates van der Waals interactions) at figure panels e, f, g, h.

Lastly, in the case of COP35 + CO_2 + N_2, there is a main CO_2 interaction domination in comparison to N_2 interactions for all studied cases (Figure 8). In 2 cases, p2 and p3, there was no N_2 BCPs recorded but only CO_2. Whereas in the case of p1, N_2 reached its highest interaction with, $\rho = 0.239 \times 10^{-2}$ a.u. and $r^2\rho = 0.399 \times 10^{-1}$ a.u. located between –N and –OH sites. Rankings of the BCPs are observed as BCP1 ⩾ BCP2 > BCP3 for both p2 and p3 cases. Among those cases, highest recorded CO_2 interaction case was obtained as $\rho = 0.247 \times 10^{-2}$ a.u. and $r^2\rho = 0.469 \times 10^{-1}$ a.u. located between =O(at CO_2) and –OH sites at p2 case. Closest distance between CO_2 and COP35 is 2.21 Å and which is higher in the case of N_2 and COP35 with 3.83 Å, Figure 7f. Furthermore, greenish-brownish isosurface color also indicates slightly stronger vDW interactions, as it is evident from the reported ρ and $\nabla^2\rho$ values.

In this work, we also explored obtaining the molecular electrostatic potential by using the MultiWFN code. The electrostatic potential (ESP) that the nuclei and electrons of a

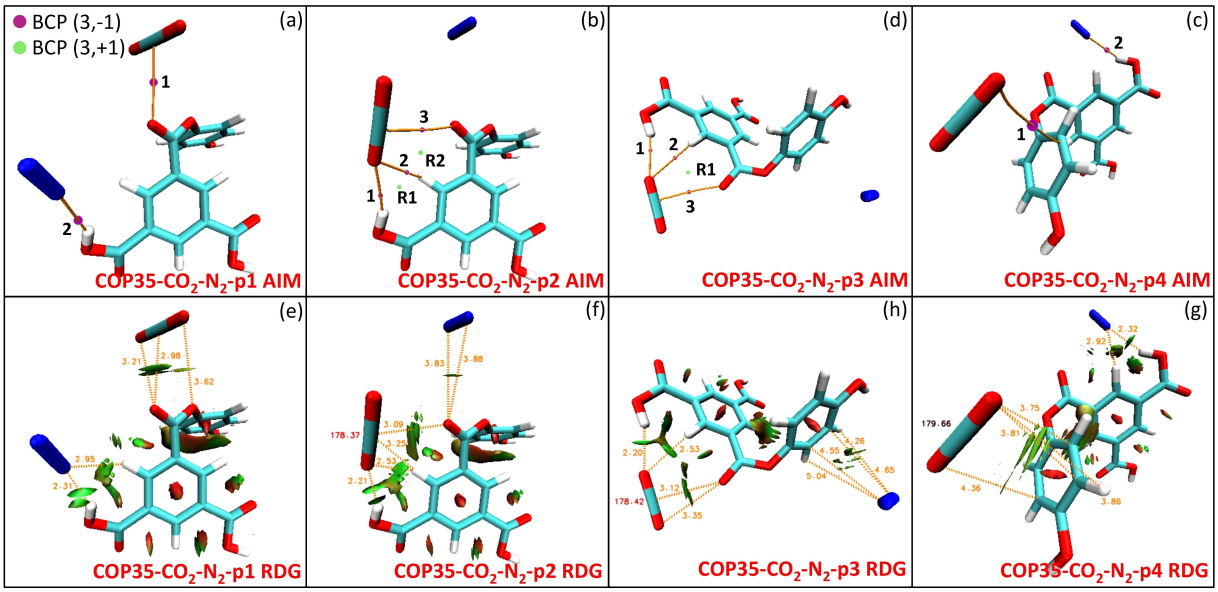

Figure 8. Atom in Molecule (AIM) analysis of COP35 interaction with CO_2 and N_2 at P1-P2-P3-P4 positions at figure panels a, b, c, d. Bond critical points (BCP) and ring critical points (RCP) involving Bond critical points (BCP) and ring critical points (RCP) involving COP35–CO_2–N_2 interactions according to AIM are shown. Reduced Density Gradient (RDG) iso-surfaces (green or green-brown color indicates van der Waals interactions) at figure panels e, f, g, h.

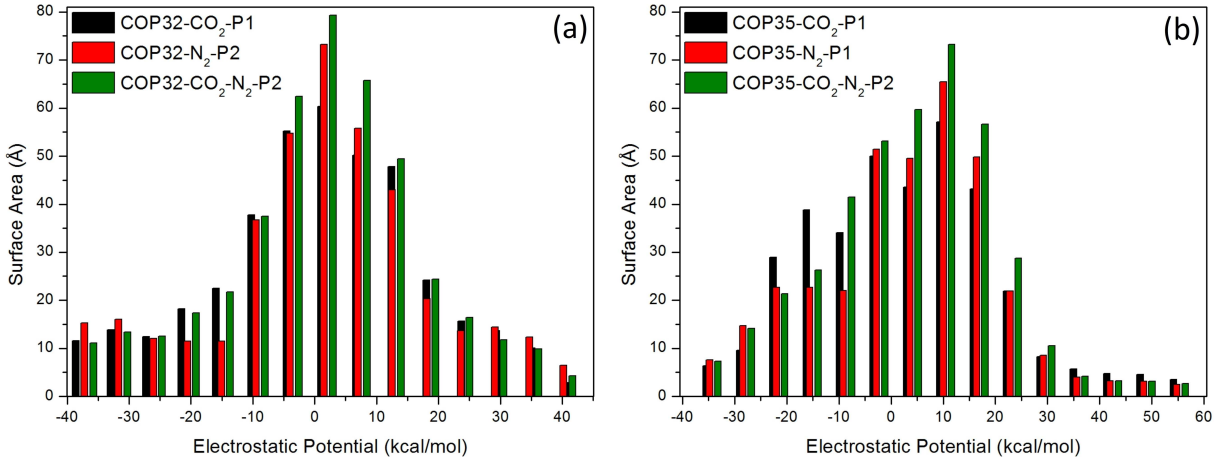

Figure 9. Electrostatic potential (ESP) distribution for given for the best CO_2, N_2 and CO_2/N_2 performance cases; (a) COP32 and (b) COP35.

molecule create in the surrounding space is well established as a guide to the interpretation and prediction of molecular reactive behavior. Furthermore, the analysis of ESP on vdW surface has also been quantified to extract the strength and orientation of weak interaction, including such as hydrogen/dihydrogen bonding and halogen bonding. These can be well predicted and elucidated by examining the scale and locations of minima/maxima on the ESP surface. Figure 9 shows ESP distribution for the best CO_2, N_2 and CO_2/N_2 performance cases. From both Figures 9a, molecular surface has well balanced and distributed ESP values close to Gaussian distribution. Whereas, in Figure 9b, it can be seen that there is a large portion of molecular surface having small ESP value, namely from −35 to 20 kcal/mol. ESP values that fall into the negative regions corresponds to: *i)* above and below benzene ring of the linker, below of benzene ring at the core and C=O site at the linker side (Figure 10a); *ii)* above and below benzene ring of the linker (Figure 10b). Low ESP regions above and below the six-membered ring and shows the effect of the abundant π-electron cloud and on the other hand the positive values dominated regions mainly arises from the positive charged C–H hydrogens; and near-neutral part represents the border area between the negative and positive parts.

As evident from Figures 10a and 10b, there are some regions that have remarkable positive and negative ESP value, corresponding to the regions closed to the global ESP minimum and maximum, respectively.

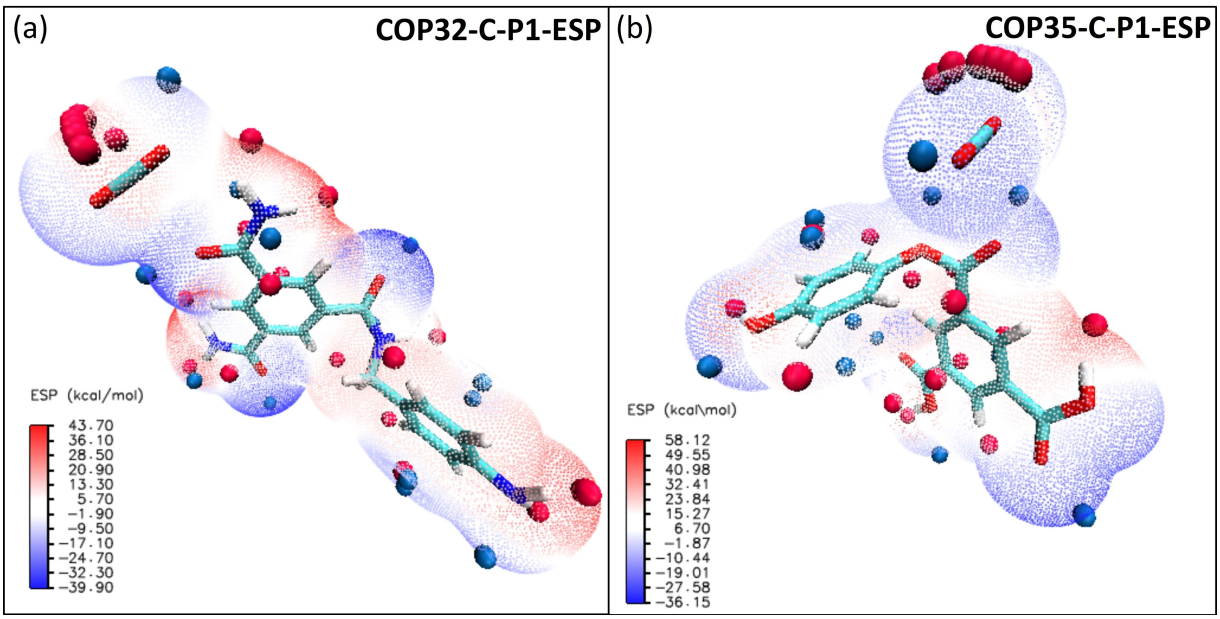

Figure 10. Color-filled molecular surface map with surface extrema for real space functions for electrostatic potential (ESP) visualization for (a) COP32-C–P1 and (b) COP35-C–P1. Blue, white and red correspond to ESP varying from −30 to 35 kcal/mol, the green and orange spheres correspond to ESP surface minima and maxima, respectively. ESP range is included in the legend at each figure panel.

Experimental studies on both COP32 and COP35 were previously published elsewhere.[62] Although comparing the DFT results with respect to experimental results would not yield vigorous and reliable results, they would provide an indication of how would be the expected trend qualitatively for each COP. Therefore we checked only ρ values for COP32 and COP35 for the highest interaction recorded cases. Considering the DFT results, one would expect CO_2 sorption performance would be considerably higher than that of N_2 sorption performance simply by considering the magnitude of the calculated electron densities for each studied case. Table S1 in ESI shows the summary of experimental performances of both the COPs and those reported results also confirms the overall adsorption performance trend of CO_2 and N_2 on both studied COPs.

For a cost efficient economic CO_2 capture and management process development, adsorption and (especially) desorption cycle mechanism of CO_2 at adsorbed surface must be examined prudently. In the case of physical adsorbents, determinations of physical limitations on desorption as important as adsorption and it is standing as one of the main hurdle for a material to be considered as viable alternative. As a cost intensive step, desorption cycle and its mechanism is investigated by studying the binding affinity COPs. There is a trade-off between the low binding energy of COPs and the CO_2 sorption performance. Lower the binding energy lower the CO_2 sorption performance, which can be modified via functionalization of the pores with the "CO_2-philic" groups in order to enhance the binding energies. It has been a widely studied fact that incorporation of polar functional groups in COP structures (and other porous structures that are designed for gas capture purposes) such as –OH, $–NH_2$ and $–NO_2$ would increase the CO_2 capture amount on COPs through stronger dipole-quadrupole interactions. In order to infer on the binding affinity of each gas on the adsorbent surface and study the binding energies experimentally, isosteric enthalpies of adsorption (Q_{st} kJ·mol^{-1}) are calculated and reported elsewhere. By studying such information, sorption performances and selectivity for different gases can be inferred. A couple of study by Sekizkardes[71] and Altarawneh[36] on benzimidazole linked COPs and their performance on binding of N_2, CO_2, and CH_4, they linked gas uptake isotherms and selectivity to binding affinity (Qst) for studied gases. Authors connected binding energy and sorption performance as lower the binding energy higher the sorption performance. Furthermore, authors also compared different gases and similar behavior is also observed on the binding energy vs sorption performance relation. A direct comparison method on the Qst and estimated binding energies via DFT calculations was studied by Rabbani[72] in a separate study. Authors used virial method and reported on the Q_{st} as it has the highest value at zero coverage then start to drop as the sorption process further progresses. One can conclude that preliminary high observed Q_{st} values are driven by favorable interactions between the active sites and the gas molecules and as these active sites become less available and accessible for the gas molecules Qst value decreases in parallel to gas loading increase. In the light of these discussions and findings, when estimated binding energies are analyzed for both COP32 and COP35 cases, one shall expect that CO_2 shall adsorb higher than N_2 on both COPs. This hypothesis was further confirmed by examining the experimental results as can be seen in Table S1, that shows for both COPs have CO_2 sorption performance is higher than the N_2 sorption performance. Although it is easier to make comparison directly from estimated DFT simulation results within the same COP compound that is

exposed to different gases at different binding sites (e.g. P1, P2 ...), in order to make comparisons on the other COPs and compare their sorption performances with simulations, one shall consider molecular dynamics (MD) simulations as it would yield more reliable basis by allowing the analysis of solvation shells together with the investigation of strong gas-COP clustering. Yet, the changes in the COP structures upon the introduction of gas molecules at different conditions (e.g. P or T) can also also be studied in MD studies in order to infer and show effective solvation of gas molecules in different COPs and observe possible volume expansion or swelling effect. Thus, in order to obtain more vigorous sorption performance comparisons, detailed molecular dynamics simulations must be conducted in order to lay down molecular arrangements.

4. Conclusions

In this DFT study, we highlighted the impact of the selection of linker molecules while forming covalent organic polymers that are designed as gas adsorbents. We investigated the interaction sites and elucidated on the experimental findings on CO_2 and N_2 sorption on these porous structures. DFT calculations were used to infer the details of the type and the strength of the polymer – gas interaction modes at various interaction sites as well as to quantify short-range interactions between the polymer – gas via topological characteristics analysis of intermolecular forces. Results obtained in this study were compared with experimental findings and confirmed the quantitative behaviour of sorption trends via considering chemical interactions and thus classification of linkers and their effect on sorption performance were explained. The reported results probes DFT as a suitable platform for in silico design of COPs for CO_2 capturing purposes through the screening of linker – CO_2 / N_2 intermolecular forces.

Supporting Information Summary

Supporting information includes, experimental and theoretical FTIR, Density of states (DOS) as a function of orbital energy, Frontier molecular HOMO and LUMO orbitals for the highest interaction energy cases for COP32 and COP35 structures.

Acknowledgement

This work was funded by Junta de Castilla y León (Spain, project BU324U14). We also acknowledge SCAYLE (Supercomputación Castilla y León, Spain) for providing supercomputing facilities. The statements made herein are solely the responsibility of the authors.

Conflict of Interest

The authors declare no conflict of interest.

Keywords: DFT · Gas Capture · Gas Storage · Porous Polymers

[1] R. Monastersky, *Nature* **2013**, *497*, 13–14.
[2] R. B. Jackson, J. G. Canadell, C. Le Quéré, R. M. Andrew, J. I. Korsbakken, G. P. Peters, N. Nakicenovic, *Nat. Clim. Change* **2015**, *6*, 7.
[3] G. P. Peters, R. M. Andrew, T. Boden, J. G. Canadell, P. Ciais, C. Le Quéré, G. Marland, M. R. Raupach, C. Wilson, *Nat. Clim. Change* **2012**, *3*, 4.
[4] *R. K. Pachauri and L. A. Meyeri, Climate Change 2014: Synthesis Report. Contribution of Working Groups I, II and III to the Fifth Assessment Report of the Intergovernmental Panel on Climate Change,* IPCC, Geneva, Switzerland, **2014**, p. 151.
[5] T. P. Senftle, E. A. Carter, *Acc. Chem. Res.* **2017**, *50*, 472–475.
[6] J. D. Steven, H. S. Robert, *Environ. Res. Lett.* **2014**, *9*, 084018.
[7] R. N. Echevarria-Huaman, T. X. Jun, *Renewable Sustainable Energy Rev.* **2014**, *31*, 368–385.
[8] D. S. Sholl, R. P. Lively, *Nature* **2016**, *532*, 435–437.
[9] United Nations Climate Change Conference, Paris, **2016**, p. 1 – 27.
[10] S. Chu, *Science* **2009**, *325*, 1599.
[11] S. Chu, Y. Cui, N. Liu, *Nature Materials* **2016**, *16*, 16.
[12] B. Smit, A.-H. A. Park, G. Gadikota, *Frontiers in Energy Research* **2014**, *55*.
[13] E. Gjernesa, L. I. Helgesena, Y. Mareeb, *Energy Procedia* **2013**, *37*, 735–742.
[14] J. Kittel, R. Idem, D. Gelowitz, P. Tontiwachwuthikul, G. Parrain, A. Bonneau, *Energy Procedia* **2009**, *1*, 791–797.
[15] J. Kittel, E. Fleury, B. Vuillemin, S. Gonzalez, F. Ropital, R. Oltra, *Mater. Corros.* **2012**, *63*, 223–230.
[16] A. Rafat, M. Atilhan, R. Kahraman, *Ind. Eng. Chem. Res.* **2016**, *55*, 446–454.
[17] A. B. Rao, E. S. Rubin, *Ind. Eng. Chem. Res.* **2006**, *45*, 2421–2429.
[18] J. Husebye, A. L. Brunsvold, S. Roussanaly, X. Zhang, *Energy Procedia* **2012**, *23*, 381–390.
[19] A. S. E. Nasr, T. Nelson, M. R. M. Abu-Zahra, *Energy Procedia* **2013**, *37*, 2432–2442.
[20] M. Vaccarelli, R. Carapellucci, L. Giordano, *Energy Procedia* **2014**, *45*, 1165–1174.
[21] G. Manzolini, E. Sanchez Fernandez, S. Rezvani, E. Macchi, E. L. V. Goetheer, T. J. H. Vlugt, *Appl. Energy* **2015**, *138*, 546–558.
[22] D. Cebrucean, V. Cebrucean, I. Ionel, *Energy Procedia* **2014**, *63*, 18–26.
[23] D. Bhattacharyya, D. C. Miller, *Curr. Opin. Chem. Eng.* **2017**, *17*, 78–92.
[24] D. J. Heldebrant, P. K. Koech, V.-A. Glezakou, R. Rousseau, D. Malhotra, D. C. Cantu, *Chem. Rev.* **2017**, *117*, 9594–9624.
[25] S. Zeng, X. Zhang, L. Bai, X. Zhang, H. Wang, J. Wang, D. Bao, M. Li, X. Liu, S. Zhang, *Chem. Rev.* **2017**, *117*, 9625–9673.
[26] G. García, S. Aparicio, R. Ullah, M. Atilhan, *Energy Fuels* **2015**, *29*, 2616–2644.
[27] S. Sarmad, J.-P. Mikkola, X. Ji, *ChemSusChem* **2017**, *10*, 324–352.
[28] S. Rafiq, L. Deng, M.-B. Hägg, *ChemBioEng Rev.* **2016**, *3*, 68–85.
[29] J. Yu, L.-H. Xie, J.-R. Li, Y. Ma, J. M. Seminario, P. B. Balbuena, *Chem. Rev.* **2017**, *117*, 9674–9754.
[30] H. Li, M. Eddaoudi, M. O'Keeffe, O. M. Yaghi, *Nature* **1999**, *402*, 276.
[31] H. A. Patel, F. Karadas, A. Canlier, J. Park, E. Deniz, Y. Jung, M. Atilhan, C. T. Yavuz, *J. Mater. Chem.* **2012**, *22*, 8431–8437.
[32] Y. Zeng, R. Zou, Y. Zhao, *Adv. Mater.* **2016**, *28*, 2855–2873.
[33] A. P. Côté, H. M. El-Kaderi, H. Furukawa, J. R. Hunt, O. M. Yaghi, *J. Am. Chem. Soc.* **2007**, *129*, 12914–12915.
[34] M. G. Rabbani, H. M. El-Kaderi, *Chem. Mater.* **2012**, *24*, 1511–1517.
[35] J. A. A. Gibson, E. Mangano, E. Shiko, A. G. Greenaway, A. V. Gromov, M. M. Lozinska, D. Friedrich, E. E. B. Campbell, P. A. Wright, S. Brandani, *Ind. Eng. Chem. Res.* **2016**, *55*, 3840–3851.
[36] S. Altarawneh, S. Behera, P. Jena, H. M. El-Kaderi, *Chem. Commun.* **2014**, *50*, 3571–3574.
[37] K. Sumida, D. L. Rogow, J. A. Mason, T. M. McDonald, E. D. Bloch, Z. R. Herm, T.-H. Bae, J. R. Long, *Chem. Rev.* **2012**, *112*, 724–781.
[38] R. Dawson, A. I. Cooper, D. J. Adams, *Prog. Polym. Sci.* **2012**, *37*, 530–563.
[39] R. S. Haszeldine, *Science* **2009**, *325*, 1647.
[40] C. J. Hawker, K. L. Wooley, *Science* **2005**, *309*, 1200–1205.
[41] G. Rabbani Mohammad, K. Sekizkardes Ali, Z. Kahveci, E. Reich Thomas, R. Ding, M. El-Kaderi Hani, *Chemistry – A European Journal* **2013**, *19*, 3324–3328.
[42] X. Feng, X. Ding, D. Jiang, *Chem. Soc. Rev.* **2012**, *41*, 6010–6022.
[43] A. H. Berger, A. S. Bhown, *Energy Procedia* **2011**, *4*, 562–567.
[44] R. P. Bisbey, W. R. Dichtel, *ACS Cent. Sci.* **2017**, *3*, 533–543.
[45] C. S. Diercks, O. M. Yaghi, *Science* **2017**, *355*.

[46] N. Huang, P. Wang, D. Jiang, *Nat. Rev. Mater.* **2016**, *1*, 16068.
[47] C. R. DeBlase, W. R. Dichtel, *Macromolecules* **2016**, *49*, 5297–5305.
[48] P. J. Waller, F. Gándara, O. M. Yaghi, *Acc. Chem. Res.* **2015**, *48*, 3053–3063.
[49] M. Dogru, T. Bein, *Chem. Commun.* **2014**, *50*, 5531–5546.
[50] J. D. Wuest, *Chem. Commun.* **2005**, 5830–5837.
[51] R. Chakrabarty, P. S. Mukherjee, P. J. Stang, *Chem. Rev.* **2011**, *111*, 6810–6918.
[52] R. Robson, *J. Chem. Soc., Dalton Trans.* **2000**, 3735–3744.
[53] H. A. Patel, S. Hyun Je, J. Park, D. P. Chen, Y. Jung, C. T. Yavuz, A. Coskun, *Nat Commun* **2013**, *4*, 1357.
[54] H. A. Patel, F. Karadas, J. Byun, J. Park, E. Deniz, A. Canlier, Y. Jung, M. Atilhan, C. T. Yavuz, *Adv. Funct. Mater.* **2013**, *23*, 2270–2276.
[55] Z. Xiang, X. Zhou, C. Zhou, S. Zhong, X. He, C. Qin, D. Cao, *Journal of Materials Chemistry* **2012**, *22*, 22663–22669.
[56] R. Gomes, P. Bhanja, A. Bhaumik, *Chem. Commun.* **2015**, *51*, 10050–10053.
[57] A. Modak, M. Pramanik, S. Inagaki, A. Bhaumik, *J. Mater. Chem. A* **2014**, *2*, 11642–11650.
[58] R. Dawson, D. J. Adams, A. I. Cooper, *Chem. Sci.* **2011**, *2*, 1173–1177.
[59] H. A. Patel, D. Ko, C. T. Yavuz, *Chem. Mater.* **2014**, *26*, 6729–6733.
[60] H. Furukawa, O. M. Yaghi, *J. Am. Chem. Soc.* **2009**, *131*, 8875–8883.
[61] H. A. Patel, S. Hyun Je, J. Park, D. P. Chen, Y. Jung, C. T. Yavuz, A. Coskun, *Nat. Commun.* **2013**, *4*, 1357.
[62] R. Ullah, M. Atilhan, B. Anaya, S. Al-Muhtaseb, S. Aparicio, H. Patel, D. Thirion, C. T. Yavuz, *ACS Appl. Mater. Interfaces* **2016**, *8*, 20772–20785.
[63] S. Adams, P. de Castro, P. Echenique, J. Estrada, M. D. Hanwell, P. Murray-Rust, P. Sherwood, J. Thomas, J. A. Townsend, *J. Cheminf.* **2011**, *3*.
[64] F. Neese, *Wiley Interdisciplinary Reviews: Comput. Mol. Biosci.* **2012**, *2*, 73–78.
[65] C. Lee, W. Yang, R. G. Parr, *Phys. Rev. B* **1988**, *37*, 785–789.
[66] A. D. Becke, *Phys. Rev. A* **1988**, *38*, 3098–3100.
[67] S. Grimme, J. Antony, S. Ehrlich, H. Krieg, *J. Chem. Phys.* **2010**, *132*, 154104.
[68] T. Lu, F. Chen, *J. Comput. Chem.* **2012**, *33*, 580–592.
[69] R. F. W. Bader, *Atoms in Molecules: a Quantum Theory*, Oxford University Press, **1990**.
[70] H. Roohi, A.-R. Nowroozi, E. Anjomshoa, *Comput. Theor. Chem.* **2011**, *965*, 211–220.
[71] A. K. Sekizkardes, S. Altarawneh, Z. Kahveci, T. İslamoğlu, H. M. El-Kaderi, *Macromolecules* **2014**, *47*, 8328–8334.
[72] M. G. Rabbani, T. Islamoglu, H. M. El-Kaderi, *J. Mater. Chem. A* **2017**, *5*, 258–265.

Submitted: June 18, 2018
Accepted: July 19, 2018